A three-level model for alkali metal vapor lasers. Part II: broadband optical pumping

Gordon D. Hager · Glen P. Perram

Abstract The effects of pump laser spectral bandwidth on the performance of longitudinally pumped diode-pumped alkali lasers is explored by extending the analytic, three-level model using longitudinally averaged number densities. By assuming a statistical distribution between the upper two levels, the limiting solution for the quasi-two level system is achieved. A second limiting solution is identified for strongly bleached conditions where the atom recycle rate, limited by spin–orbit relaxation, fully specifies the output power. Performance in the intermediate regime depends significantly on the pump bandwidth relative to the atomic absorption line width and requires numerical simulation. The ratio of populations for the two excited, $^2P_{3/2,1/2}$ states completes an analytic solution and depends primarily on pump laser bandwidth, threshold, and alkali concentration. Absorption well into the wings on the atomic profile can be utilized by increasing alkali concentration, but imposes increased pump intensity threshold.

1 Introduction

Diode-pumped alkali metal vapor lasers (DPAL) offer significant promise for high average power performance [1]. The radiation from the un-phased diode lasers are absorbed on the D_2 line, $^2S_{1/2} \rightarrow {}^2P_{3/2}$, collisional relaxation populates the lower $^2P_{1/2}$ state, and lasing is achieved on the $^2P_{1/2} \rightarrow {}^2S_{1/2}$ transition. For example, a rubidium laser pumped by a 1.28-kW diode stack with a 0.35-nm bandwidth has achieved 145-W average power [2]. More recently, Russian workers [3] have reported a closed loop transverse flow cesium laser that achieved approximately 1 kW of laser output power. The laser cell was pumped co-axially with the laser axis from each side using two diode bar arrays each producing 1 kW. The optical-to-optical efficiency in this device was 48 %.

Slope efficiencies of greater than 80 % have been achieved when the pump and resonator volumes are mode matched and a high fraction of the incident pump radiation is absorbed [4]. The spectral width of the diode sources of $\sim$1,000 GHz is typically much larger than the atomic absorption profile of $\sim$10 GHz at 1 atm. A number of laser demonstrations have used single narrow-band diodes, partially narrow banded low-power diode arrays, and surrogate pump sources such as CW Ti–Sapphire lasers or pulsed dye lasers [1–12]. Alternatively, high-pressure $\sim$20 atm gas cells may be employed [13]. Absorption for broadband pumps can be increased well into the wing of the atomic line shape by increasing the alkali concentration, but at the expense of increased threshold [11]. Assessing the effects of pump lineshape on DPAL system performance is the subject of the present modeling effort.

Several DPAL models have been developed, including the pioneering work by Beach [6]. Two recent studies that consider broadband optical pumping have been reported by Zameroski et al. [11] and Yang et al. [14, 15]. The work reported by Zameroski [11] involved an extensive experimental and theoretical study of a repetitively pulsed Rb DPAL system in which the pump band width is approximately a factor of two greater than the width of the absorption transition. Very good

G. D. Hager · G. P. Perram (✉)
Department of Engineering Physics, Air Force Institute of
Technology, 2950 Hobson Way, Wright-Patterson Air Force
Base, OH 45433, USA
e-mail: glen.perram@afit.edu

agreement between a numerical time-dependent rate equation model and experimental results was obtained. The work reported by Yang [14, 15] considered a CW longitudinally pumped DPAL configuration in which both longitudinally dependent number densities and broadband pumping were taken into account. The rate equations were solved numerically. Yang and his coworkers [14, 15] compared their results with the original Beach model [6] that used longitudinally averaged number densities for a specific case. The results of this comparison showed that for a two-pass pump configuration the difference in predicted laser output power between the two models deviated by about 6 % at threshold and decreased rapidly as the pump power increased. For pump powers greater than approximately three times the threshold value the two models give results that were within 1 %. Other recently reported studies include the effects of temperature gradients [16], transverse pumping geometries [14], and radial intensity distributions [11].

We previously reported in part I [17] an analytic three-level model using the longitudinally averaged number densities approach previously developed for solid-state lasers [18, 19]. In this paper, we extend this solution methodology to include the more general case of broadband pumping. We first solve the steady-state rate equations algebraically. The intermediate solutions to the rate equations are analytic functions of the longitudinally average pump rate Ω_f, (Sects. 2, 4), which depends on the frequency distribution of the pump. Because of the pump frequency dependence the general solutions of the DPAL rate equations are numerical.

We also provide an alternative formulation of the DPAL equations that is algebraic. This formulation provides a great deal of insight and provides a direct path to determine both the quasi two-level limit and the maximum laser power limit for complete pump bleaching in the general broadband pumping case. We note that DPALs in general achieve their highest efficiency in the linear slope region described by the quasi two-level limit. In the parameter space between the quasi two-level and maximum power limits the rate equations are solved numerically.

The remainder of the paper is organized as follows: Sect. 2 provides a discussion of the model. In Sect. 3 the alternative analytic description of the DPAL equations is given. In Sect. 4 the results of Sect. 3 are applied in the determination of equations that describe quasi two-level and bleached DPAL limits. Section 5 gives a discussion of the numerical solution procedure and results. Section 6 gives the conclusions. We present the analytic model results first because the numerical results are best interpreted with an understanding of quasi two-level and bleached high-power limits.

2 Model development

2.1 Cavity geometry

The geometry for an end-pumped DPAL system is shown schematically in Fig. 1. The diode pump beam may be injected into the stable, standing wave cavity through a dichroic mirror or beam splitter. The intensity of the pump beam, just before entering the alkali vapor cell from the left, is denoted, I_p. The pump beam may be reflected from mirror M_2 with reflectivity, r_p, for a second pass through the gain media of length, l_g. The present model assumes no radial variation for the pump beam intensity. The cell windows may be at Brewster's angle to reduce transmission losses, t_p and t, for the pump and laser beams, respectively. The output coupler on the left side of the resonator has a reflectivity at the laser wavelength of r. The DPAL gain is high, and optimum performance is usually achieved for a low-finesse cavity. We assume the reflectivity of M_2 at the DPAL wavelength is 100 %. For the baseline cavity design provided in Table 1, the round trip loss, which is equal to the threshold gain, is given by

$$\alpha = g_{th} = \frac{-1}{2l_g} \mathrm{Ln}(rt^4) \tag{1}$$

or $\alpha = 0.214$ cm^{-1}.

2.2 Rate equations

The three energy levels for the alkali laser system are illustrated in Fig. 2. The diode pump radiation is tuned to the $^2S_{1/2} \rightarrow {}^2P_{3/2}$ transition, collisional relaxation, with decay rate γ, populates the upper laser, $^2P_{1/2}$, and inversion is achieved with respect to the ground state. The optical properties for the baseline Rb DPAL system are summarized in Table 1. The Rb fine structure splitting is relatively small, $E_3 - E_2 = 237.596$ cm^{-1}. The pump and lasing wavelengths are similar, $\lambda_p = 780.241$ nm and $\lambda_L = 794.797$ nm, yielding a high quantum efficiency, $\eta_{qe} = h\nu_L/h\nu_p = \lambda_p/\lambda_L = 0.981$. Electronic squenching by most buffer gases is very slow [20], so that the total decay rates from both excited levels, Γ_{31} and Γ_{21}, are dominated by spontaneous emission with rates $\Gamma_{31} \cong A_{31} = 3.81 \times 10^7$ and $\Gamma_{21} \cong A_{21} = 3.61 \times 10^7$ s^{-1} [21]. The degeneracies, $g_1 = 2$, $g_2 = 2$, and $g_3 = 4$, favor depopulation of the ground state. The pressure broadened absorption and emission lines are assumed to be spectrally homogeneous.

The rate equations for the three-level diode-pumped alkali laser system were developed for narrow-band pumping in the first of these papers [17]. Extending the analysis to the broadband pumping case requires modification. The longitudinally averaged densities in the ground $^2S_{1/2}$, the upper laser $^2P_{1/2}$, and pumped $^2P_{3/2}$ states, n_1, n_2,

Fig. 1 Longitudinally pumped laser cavity and gain cell. The input pump intensity, I_p might be injected from a polarizing beam splitter or through a dichroic mirror. The DPAL output intensity, I_L, is obtained through the output coupler, M_1
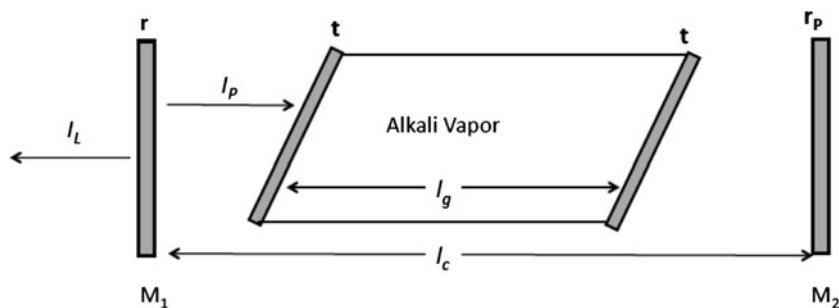
Table 1 Definition of key symbols and baseline gain conditions

Variable	Value	Definition
l_g	4 cm	Gain length
t	0.975	Window transmission
t_p	1	Window transmission at pump wavelength
r_p	1.0	Reflectivity of back mirror, M_2 at pump wavelength
r	0.2	Reflectivity of output coupler, M_1 at laser wavelength
$\alpha = g_{th}$	0.214 cm^{-1}	Cavity loss (threshold gain)
T_c	0.937	Cavity transmission
λ_p	780.24 nm	Pump wavelength
λ_L	794.98	Laser wavelength
η_{qe}	0.981	Quantum efficiency
ΔE_{32}	237.596 cm^{-1}	Fine-structure splitting
A_{31}	3.81×10^7 s^{-1}	Spontaneous emission rate for pumped level
A_{21}	3.61×10^7 s^{-1}	Spontaneous emission rate for upper laser level
n	2×10^{13} cm^{-3}	Total rubidium concentration
[CH$_4$]	1.9×10^{19} cm^{-3}	Methane concentration
[He]	1.5×10^{19} cm^{-3}	Helium concentration
T	393 K	Gain cell temperature
Δv_p	19.7 GHz	Pump bandwidth (FWHM)
Δv_{31}	19.7 GHz	Atomic absorption homogeneous linewidth (FWHM)
$\sigma_{31}(v_p)$	2.98×10^{-13} cm^2	Cross-section for stimulated emission on pump transition
$\sigma_{21}(v_L)$	2.93×10^{-13} cm^2	Cross section for stimulated emission on lasing transition
I_s	32.7 W/cm^2	Saturation intensity
$2e^{-\theta}$	0.84	Detailed balance ratio
$g_{th}/\sigma_{21}n$	0.039	Normalized threshold
κ	160	Ratio of spin–orbit mixing and radiative rates
χ_b	1.74	Excited states population ratio in the bleached limit

and n_3, respectively, and the longitudinally averaged two way laser circulating intensity Ψ are determined from four linearly independent steady-state rate equations:

$$\frac{dn_1}{dt} = 0 = \frac{-\Omega_f}{hv_p} + \sigma_{21}(n_2 - n_1)\frac{\Psi}{hv_L} + n_2\Gamma_{21} + n_3\Gamma_{31} \quad (2)$$

$$\frac{dn_2}{dt} = 0 = -\sigma_{21}(n_2 - n_1)\frac{\Psi}{hv_L} + \gamma(n_3 - 2e^{-\theta}n_2) - n_2\Gamma_{21} \quad (3)$$

$$n = n_1 + n_2 + n_3 \quad (4)$$

$$\frac{d\Psi}{dt} = 0 = \sigma_{21}(n_2 - n_1) - \alpha \quad (5)$$

In Eq. (2), Ω_f is the longitudinally averaged two-way pump intensity. The total population n in Eq. (4) is assumed to be constant with no population transferred to higher lying alkali states. The rate equations (2–5) are the same as in part I [17] with the exception that the first term on the right-hand side of Eq. (2) is modified to account for the fact that the pump is broad band and must be treated differently than in the single-frequency pump results of part I [17]. The intermediate algebraic solutions of the steady-state rate equations (2–5) are analytic functions of the parameter, Ω_f. There are two solution branches to the rate equations. The small signal gain branch solutions are obtained by setting $\Psi = 0$ and solving Eqs. (2)–(4) simultaneously for n_1, n_2, and n_3. For the lasing branch all four linearly independent equations are required and solved simultaneously to obtain n_1, n_2, n_3, and Ψ. Equation (5) of the lasing branch solutions insures that the loaded gain is clamped at its threshold value. For completeness and easy reference the intermediate algebraic solutions of the rate equations for the small signal and lasing branches are listed in Appendix 1. In Appendix 2 we provide a derivation of the pump term, Ω_f, in Eq. (2).

A summary of the model notation, parameters, and baseline values for Rb is reported in Table 1. We choose a total Rb concentration of $n = 2.0 \times 10^{13}$ atoms/cm^3. A methane concentration of 1.9×10^{19} cm^{-3}, corresponding to 600 Torr at 300 K, is used to induce rapid fine structure mixing, establishing a decay rate of $\gamma = 6.11 \times 10^9$ s^{-1} [22]. The rates for collisional transfer between the fine structure states, $\gamma = k_{32}[CH_4]$, are related by detailed balance, $k_{23} = 2e^{-\theta} k_{32}$, where $\theta = \Delta E_{32}/k_B T = 0.87$ for Rb at $T = 393$ K. The longitudinally averaged, intra-cavity
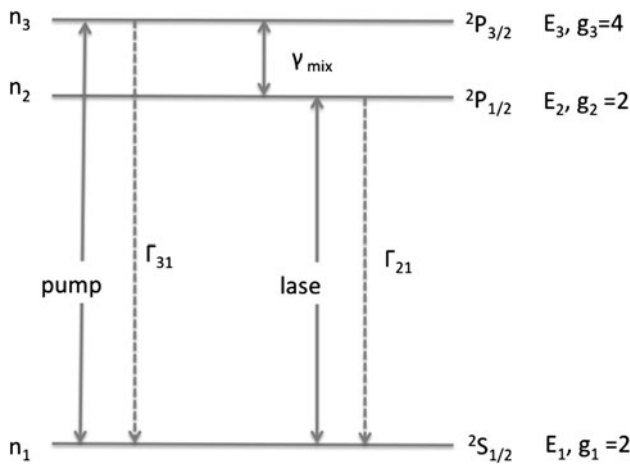
Fig. 2 DPAL energy level diagram illustrating optical pumping, fine structure mixing, radiative, and lasing processes

pump, Ω_f, and lasing, Ψ, intensities are discussed below. Further details regarding the rate equations and energy levels involved are provided in the prior work [17].

2.3 Broadband pump rate

The longitudinally averaged intra-cavity pump intensity for two passes, assuming no transmission losses and perfect reflection, is modified by the spectral width of the pump, Appendix 2 [17].

$$\Omega_f = \frac{I_p}{l_g}\left(\int_{-\infty}^{\infty} f_p(v)e^{\sigma_{31}(v)(n_3(\Omega_f)-2n_1(\Omega_f))2l_g}dv - 1\right) \quad (6)$$

The number densities in Eq. (6) are explicit functions of Ω_f. Equation (6) is a transcendental integral equation that is solved numerically. The solutions of Eq. (6) determine the longitudinally averaged pump intensity for each value of the independent input variable I_p.

The pump spectral intensity is assumed to be Gaussian:

$$f_p(v) = \left(\frac{2(\ln 2)^{1/2}}{\pi^{1/2}\Delta v_p}\right)\exp\left[-4\ln 2\left(\frac{v-v_p}{\Delta v_p}\right)^2\right] \quad (7)$$

with a width (FWHM) of Δv_p. Equation (6) simply expresses the overlap of the spectrally broad pump with the atomic absorption feature and follows directly from Eq. (4) of reference [17]. The absorption profile in general depends on temperature, pressure broadening, collision induced shifts, and the hyperfine splitting [23], and at low pressures is represented by a set of closely spaced overlapping Voigt functions. However, the absorption cross-section

$$\sigma_{13}(v) = 2\sigma_{31}(v) = 2\frac{\lambda_p^2}{8\pi}A_{32}f_{31}(v) \quad (8)$$

at pressures near 1 atm may be adequately characterized by a single Lorentzian lineshape:[24].

$$f_{31}(v) = \frac{1}{2\pi}\frac{\Delta v_{31}}{((v-v_p)^2+(\Delta v_{31}/2)^2)} \quad (9)$$

The cross-section for the 2-1 lasing transition in the rate equations (2–5) is evaluated at line center $\sigma_{21} \equiv \sigma_{21}(v_L)$.

In addition to methane, a baseline helium concentration of 1.5×10^{19} atoms/cm^3 is used to pressure broaden the pump transition for a homogenous linewidth (FWHM) of $\Delta v_{31} = 19.7$ GHz [23]. The cross-sections for pump absorption, $\sigma_{13} = 2\sigma_{31}$, and laser-stimulated emission, σ_{21}, are evaluated at line center in Table 1. A plot of the area normalized spectral distributions for the 19.73-GHz pump and pressure-broadened D$_2$ transition is shown in Fig. 3. The saturation intensity is defined for the pump transition as

$$I_s = \frac{hv_p}{\sigma_{31}}\Gamma_{31} \quad (10)$$

2.4 Lasing intensity

A full analysis of the right- and left-traveling, intra-cavity pump and laser intensities, and their relationship to the incident pump intensity was presented in the first paper [17]. The output laser intensity, I_L, is related to the single-frequency longitudinally averaged two-way laser circulating intensity, Ψ, as previously developed:

$$\Psi = I_l\frac{(e^{g_{th}l_g}-1)(1+t^2re^{g_{th}l_g})}{g_{th}l_gt(1-r)e^{g_{th}l_g}} \quad (11)$$

The lasing intensity grows from axially directed spontaneous emission once the small signal gain reaches the threshold value. Once lasing is achieved the loaded gain remains clamped at the threshold value. The quantities Ψ and Ω_f are determined from the numerical solutions of Eq. (6) together with the intermediate algebraic solutions, Appendix 1 and provide the complete numerical solutions for both the small signal and lasing branches.

3 Laser cycling rates

The DPAL system converts un-phased pump photons from the diode bars to a single coherent beam by rapidly cycling the alkali atoms through the pump, spin–orbit relaxation, and lasing processes. In steady state, the output power will be limited by the slowest of these steps. In the quasi two-level limit, the spin–orbit relaxation is assumed to be very fast, and output power is limited by the pump rate, and increases linearly as the pump intensity increases. When the spin–orbit relaxation is rate limiting, the pump
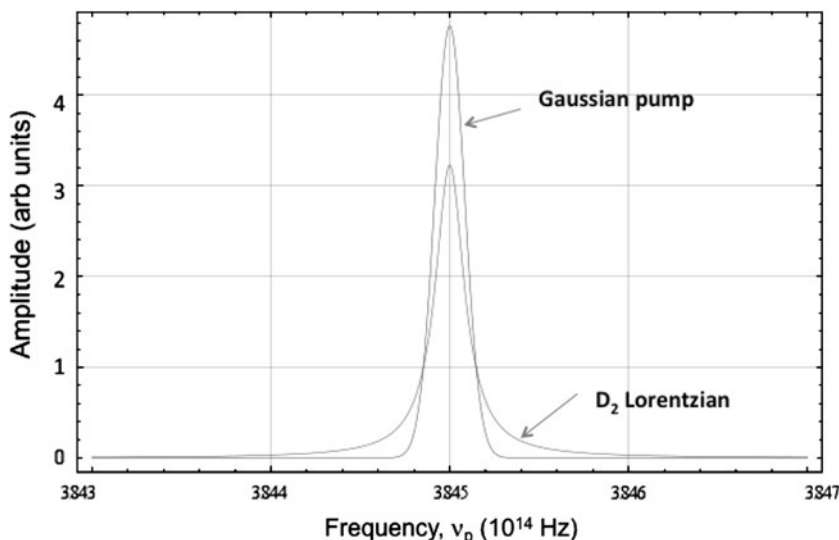
transition becomes fully bleached, excess pump intensity is transmitted, and output power is limited by the spin–orbit relaxation rate. Analytic solutions in these two limits exist due to the fact that the number densities in the rate equations are completely fixed in these limits. The results for the fully bleached limit are independent of pump bandwidth. The detailed transition between linear quasi two-level behavior and the bleached limit requires numerical solution as discussed below.

The pump rate, first term on the right-hand side of Eq. (2), gives the total rate of population transfer from level 1 to level 3 for all frequencies contained in the pump. Once in level 3, in the absence of quenching, this population density can return to level 1 by lasing or by spontaneous emission to level 1 from levels 3 and 2. Subtracting the spontaneous emission contribution from the first term on the right-hand side of Eq. (2) and substituting Eq. (6) for Ω_f gives the fraction of the pump rate that returns to level 1 by lasing. We denote this quantity by P:

$$P = \frac{I_p}{h\nu_p l_g}\left(1 - \int_{\infty}^{-\infty} f_p(\nu)e^{\sigma_{31}(\nu)(n_3(\Omega_f)-2n_1(\Omega_f))2l_g}d\nu\right) - \Gamma_{31}n_3 - \Gamma_{21}n_2 \qquad (12)$$

The total population transfer rate between level 3 and level 2 is given by the second term on the right-hand side of Eq. (3). Once in level 2 the population density can return to level 1 by lasing or by spontaneous emission from level 2 to level 1. Subtracting the spontaneous emission term from the total 3 to 2 population transfer rate gives the fraction of the transfer rate that returns to level 1 by lasing. We denote this rate by M:

$$M = \gamma(n_3(\Omega_f) - 2e^{-\theta}n_2(\Omega_f)) - \Gamma_{21}n_2) \qquad (13)$$

Finally, the lasing rate L is determined from the threshold condition:

$$L = g_{th}\frac{\Psi}{h\nu_L} \qquad (14)$$

The significance of these three rate processes, defined by Eqs. (12–14), lies in the fact that in steady state all three rates are all equal, $(P = M = L)$, and from this equivalence we can derive limiting solution forms without the need to solve Eqs. (2–5, 6).

An expression for the output laser intensity is determined by substituting Eq. (11) into Eq. (14) and equating the result to Eq. (12). After rearrangement the following result is obtained:

$$I_L = \left(\frac{\nu_L}{\nu_p}\right)\left(\frac{t(1-r)e^{g_{th}l_g}}{(e^{g_{th}l_g}-1)(1+t^2re^{g_{th}l_g})}\right)$$
$$\left[I_p\left(1 - \int_{-\infty}^{\infty} f_p(\nu)e^{\sigma_{31}(\nu)(n_3(\Omega_f)-2n_1(\Omega_f))2l_g}d\nu\right)\right.$$
$$\left. - (\Gamma_{31}n_3 + \Gamma_{21}n_2)h\nu_p l_g\right] \qquad (15)$$

Threshold is specified by the spontaneous emission term. The slope efficiency depends on the quantum efficiency, cavity losses, and the fraction of the pump intensity absorbed. The absorption term attains its maximum value for a certain linear range above threshold where the number densities can be determined from the quasi two-level equations. A maximum value approaching one for the absorption term is attained when the pump bandwidth is less than the D_2 absorption line width and decreases as the pump bandwidth increases. As the pump bandwidth increases the maximum fractional

absorption decreases. This is due to the fact that power contained in the wings of the pump is transmitted and not effective in pumping the D_2 transition.

To simplify the notation we write the absorption term as

$$\beta = 1 - \int_{-\infty}^{\infty} f_p(v) e^{\sigma_{31}(v)(n_3(\Omega_f) - 2n_1(\Omega_f))2l_g} dv \tag{16}$$

so that the laser intensity becomes

$$I_L = \eta I_p - I_{th} \tag{17}$$

where the slope efficiency is

$$\eta = \eta_{qe} \beta T_c \tag{18}$$

and the cavity transmission is

$$T_c = \frac{t(1-r)e^{g_{th}l_g}}{(e^{g_{th}l_g} - 1)(1 + t^2 r e^{g_{th}l_g})} = \frac{t(1-r)}{(1+\sqrt{r})(1 - t^2\sqrt{r})} \tag{19}$$

The threshold gain of Eqs. (1, 11) has been used to simplify the second expression for Eq. (19). The cavity transmission is $T_c = 1$ for no window losses, $t = 1$. The lasing threshold is defined in terms of the pump saturation intensity, I_s, of Eq. (10) as

$$I_{th} = I_s \eta_{qe} \left[\sigma_{31} l_g \left(n_3 + n_2 \frac{\Gamma_{21}}{\Gamma_{31}} \right) \right] T_c \tag{20}$$

4 Quasi two-level and bleached limits

The absorption term, β, is a function of the pump intensity due to the bleaching of the populations, as described in Eq. (16). For very strong pump intensities the D_2 transition is fully bleached and $n_3(\Omega_f) - 2n_1(\Omega_f) \to 0$. In this fully bleached limit, the exponential in the integrand of Eq. (16) is nearly unity and $\beta \to 0$. Alternatively, if the fine structure mixing rate is very rapid relative to the pump rate, $\beta \to 1$, and all the pump photons are absorbed. In this quasi two-level limit, the spin–orbit mixing rate is infinite and the population ratio for the two excited states

$$\chi = n_3(\Omega_f)/n_2(\Omega_f) \tag{21}$$

is statistical:

$$\chi_{Q2L} = 2e^{-\theta} \tag{22}$$

In the quasi two-level limit, the population ratio, χ, is minimized. For finite fine structure mixing and strong pumping, the ratio increases, a smaller fraction of the pump photons are absorbed, and slope efficiency declines.

It is instructive to consider the populations in the three alkali states as a function of optical losses (threshold gain, $g_{th} = \alpha$), total alkali concentration, n, and the population

ratio, χ. When the gain is clamped to the losses, Eq. (1), and the ratio of populations in the two excited states is represented by Eq. (21), the populations are parametrically described as

$$n_1(n, g_{th}, \chi) = \frac{n - \frac{g_{th}}{\sigma_{21}}(1+\chi)}{2+\chi} \tag{23}$$

$$n_2(n, g_{th}, \chi) = \frac{n + \frac{g_{th}}{\sigma_{21}}}{2+\chi} \tag{24}$$

$$n_3(n, g_{th}, \chi) = \frac{\chi\left(n + \frac{g_{th}}{\sigma_{21}}\right)}{2+\chi} \tag{25}$$

The value for the population ratio, χ, depends principally on the intra-cavity pump intensity, Ω_f, and the fine structure mixing rate, γ. The solutions to the rate equations (2–5) can be summarized by the excited population ratio:

$$\chi(\Omega_f) = 2 \frac{\left(1 + \frac{g_{th}}{n\sigma_{21}}\right) k e^{-\theta} + \left(1 - \frac{g_{th}}{n\sigma_{21}}\right)\left(\frac{\Omega_f}{I_s}\right)}{\left(1 + \frac{g_{th}}{n\sigma_{21}}\right)(1+k) + \left(1 + 3\frac{g_{th}}{\sigma_{21}}\right)\left(\frac{\Omega_f}{I_s}\right)} \tag{26}$$

where the fine structure mixing rate has been expressed relative to the radiative rate, $\kappa = \gamma/\Gamma_{31}$.

A plot of the excited state population ratio of Eq. (26) for several gain cell conditions is provided in Fig. 4. For large spin orbit relaxation, $\kappa \to \infty$, or low pump intensity, $\Omega_f/I_s \to 0$, the quasi two-level (Q2L), ideal limit of Eq. (26) yields

$$\lim_{k \to \infty} x = \lim_{x \to \infty} x = 2e^{-\theta} \equiv x_{Q2L} \tag{27}$$

For rubidium at $T = 393$ K, the quasi two-level limit is $\chi_{Q2L} = 2e^{-\theta} = 0.84$. The larger spin–orbit splitting for Cs yields a smaller limiting value of $\chi_{Q2L} = 0.19$. Indeed, the fraction of the alkali concentration contributing to the gain, $(n_2(\Omega_f) - n_1(\Omega_f))/n$, in the quasi two-level limit increases from 0.07 to 0.70 as we move from K to Cs DPAL variants. Substituting the quasi two-level number densities into Eq. (15) and noting that $\beta(n, g_{th}, \chi_{Q2L})$ approaches a value of one when the pump bandwidth is less than the D_2 absorption bandwidth, we obtain the single-frequency quasi two-level equations of Part I [17].

If the mixing rate is finite, the pump transition will saturate for higher input pump intensity. We note that the quantity $n_3(\Omega_f) - 2n_1(\Omega_f)$ is always less than or equal to zero. For complete saturation of the pump transition the upper limit for the population ratio, χ_s, is determined by finding the value of χ that satisfies

$$n_3(n, g_{th}, x) - 2n_1(n, g_{th}, x) = 0 \tag{28}$$

or

$$x_b \equiv \lim_{\Omega_f \to \infty} \frac{n_3}{n_2} = \frac{2\left(1 - \frac{g_{th}}{n\sigma_{21}}\right)}{\left(1 + 3\frac{g_{th}}{n\sigma_{21}}\right)} \tag{29}$$

Using the baseline values of n, g_{th}, and σ_{21} as defined in Table I, the fully bleached value of $\chi_b = 1.74$ is obtained. This limit is achieved at lower pump intensity for lower fine structure mixing rates, as seen in behavior of the $\kappa = 10$ curve in Fig. 4. An upper limiting value of 2 for χ_b could in principle be obtained by forcing g_{th} to approach zero. This could be accomplished either by increasing the gain length or by increasing the reflectivity of the out coupling mirror or a combination of both.

The maximum absorbed pump intensity, I_a^{max}, and maximum laser intensity, I_L^{max}, for given alkali and buffer gas concentrations are achieved in the asymptotic limit of complete pump bleaching. These expressions are obtained by equating the transfer rate, Eq. (14), to the pump rate, Eq. (13), giving the maximum intensity absorbed and equating the mixing rate to the lasing rate, Eq. (15), and using Eq. (11). These expressions, evaluated with $\chi = \chi_b$ (the bleached limit), are given by

$$I_a^b = h\nu_p l_g \{\gamma[n_3(n, g_{th}, x_b) - 2n_2(n, g_{th}, x_b)e^{-\theta}] + \Gamma_{31}n_3(n, g_{th}, x_b)\} \quad (30)$$

$$I_L^b = h\nu_L l_g T_c \{\gamma[n_3(n, g_{th}, x_b) - 2n_2(n, g_{th}, x_b)e^{-\theta}] + \Gamma_{31}n_3(n, g_{th}, x_b)\} \quad (31)$$

We note that χ_b, and thus the asymptotic laser intensity, does not depend on the pump bandwidth. Using the bleached limit value for the population ratio of Eq. (29) and neglecting the second, spontaneous term in Eq. (31), yields a laser intensity of

$$I_L^b = h\nu_L T_c \gamma l_g \left(\frac{1 - e^{-\theta}}{2}\right) n \quad (32)$$
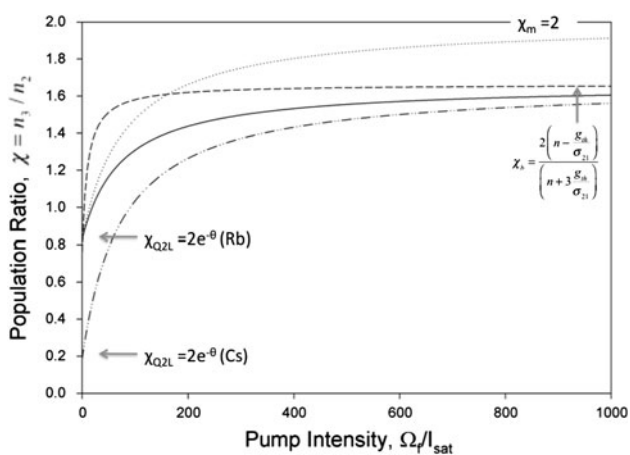

Fig. 4 Population ratio for the two excited states, $\chi = n_3/n_2$, as a function of longitudinally averaged, intra-cavity pump intensity. Three Rb cases: (*solid lines*) baseline conditions of Table 1, (*dashed lines*) for $\kappa = 10$, and (*dotted lines*) for $g_{th} = 0$, and one Cs case: (*dashed dotted lines*) $\theta = 2.4$, are shown

The factor involving the fine structure splitting, $(1 - e^{-\theta})/2$, provides the fraction of alkali concentration contributing to the laser output power. As the splitting becomes small (light alkali atoms) the laser approaches a two-level system, with no output power.

In a recent experiment, a pulsed Rb laser operated at pump intensities exceeding 3.5 MW/cm^2 is clearly in the highly bleached limit. [10] The output energy is linearly dependent on pump pulse duration for a given pump energy. The ethane concentration of 1.8×10^{19} cm^{-3} limits the recycle rate and the laser can only process about 50 photons/atom during the 2–8 ns pump pulse. Indeed, the results are consistent with Eq. (32), where the number of alkali atoms cycled per second is in proportion to γn. The experimental optical-to-optical efficiency based on absorbed photons approaches 36 % even for these extreme pump conditions.

The output intensity scales linearly with input intensity in the quasi-two-level limit. For a radially uniform pump intensity, as the current flat-top pump intensity model assumes, there is always some linear, quasi two-level regime near threshold. Upward curvature in the output intensity plot has been observed and attributed to the radial distribution of pump intensity for small pump area experiments [11]. Using the population distribution among the three levels, Eqs. (23–25) for the Q2L limit of Eq. (27), leads to a predicted output intensity from Eq. (16) of

$$I_L^{Q2L} = \left(\frac{\nu_L}{\nu_p}\right) T_c I_p - I_{th} \quad (33)$$

All absorbed photons (above threshold) can be converted to output photons in the quasi two-level limit, if the cavity is lossless, $T_c = 1$, and the resonator extraction is ideal (mode volume overlap is unity, see reference [17]). If the mode overlap is less than unity, (as is the case in many small-scale experiments where the laser and pump beams vary spatially in the transverse plane), Eq. (33) can be modified by multiplying the slope by η_{mode}.

5 Numerical solutions to the rate equations

5.1 Longitudinally averaged, broadband pump intensity

The numerical solution is completed by determining the value of the longitudinally averaged, broadband pump intensity, Ω_f as a function of the input pump intensity. The concentrations of the three levels are determined from the intermediate algebraic solutions of Eqs. (2–5), Appendix 1, and are functions of Ω_f. The definition of the average pump intensity of Eq. (6), with the concentrations dependent on pump intensity, represents a transcendental equation with

input pump intensity as the key parameter. The numerical procedure is to find the root of the transcendental Eq. (6) for each value of I_p over the range of I_p values of interest. The set of pairs, $\{I_p, \Omega_f\}$, with I_p as the independent variable defines the numerical functional relationship between the input pump intensity and the dependent variable Ω_f:

$$\Omega_f = F(I_p) \tag{34}$$

Typical results for the solution of Eq. (34) for the narrow-band pumped case were previously discussed [17]. Figure 5 compares the relationship between incident pump intensity, I_p, and longitudinally averaged intra-cavity intensity, Ω_f, for the baseline conditions reported in part I [17] at several pump band widths. Two curves for the narrow-bandwidth pump solution are provided: with and without lasing. In the absence of lasing, and at low intensity, the pump is fully absorbed before a single pass and the longitudinal average is low. When I_p reaches about 0.2 kW/cm², the sample becomes fully bleached and Ω_f increases due to the reflected pump beam. At higher pump intensities, $I_p > 1$ kW/cm², the slope of the curve approaches 2 due to the pump's double pass. An expanded view of the narrow band, no lasing solution was provided in part I [17]. In the presence of lasing, the longitudinally averaged pumped intensity remains low even at 4 kW/cm². With lasing, cycling in the three-level system is complete and many pump photons can be converted to laser output. Only when the fine structure mixing rate limits the cycling can a significant fraction of the pump intensity be transmitted. Figure 5 also shows a solution to the transcendental Eq. (34) for a $\Delta v_p = 100$ GHz pump linewidth. Less power is extracted for the broadband pump at a fixed Rb concentration, particularly near threshold. Little curvature is evident in the high bandwidth solution, reflecting the large range of absorption across the pump spectral distribution. As seen below, the transition from quasi two-level ideal behavior to the fully bleached limit is more gradual for a broadband pump.

In order to more completely interpret the computational results, the following additional functions are defined in terms of Eq. (34). The total input pump intensity absorbed in a double pass through the gain cell is given by

$$I_a(I_p) = I_g F(I_p) \tag{35}$$

The spectral distribution of the transmitted pump intensity after a double pass through the gain cell is given by

$$I_t(v, I_p) = I_p f_p(v) e^{\sigma_{31}(v)(n_3(F(I_p)) - 2n_1(F(I_p)))2l_g} \tag{36}$$

The frequency integral of Eq. (36) gives the total intensity that escapes after a double pass through the cell:

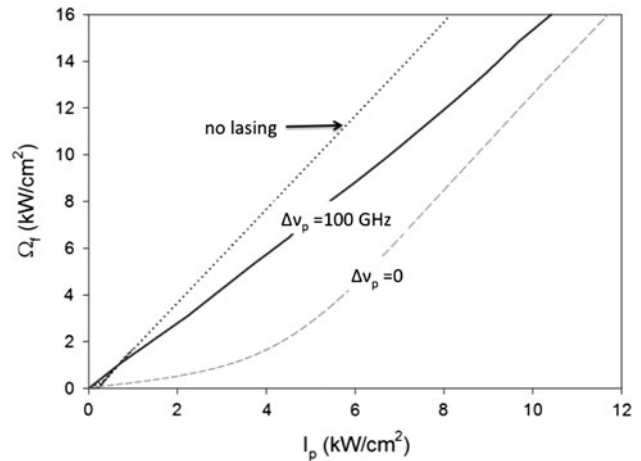$$I_t(I_p) = \int_{-\infty}^{\infty} I_t(v, I_p) dv \tag{37}$$

Fig. 5 Longitudinally average intra-cavity intensity as a function of input pump intensity for the conditions of reference [17] for (*dashed lines*) narrow-band pumping with and (*dotted lines*) without lasing, and (*dashed dotted lines*) a 100 GHz pump bandwidth with lasing

The pump intensity absorbed and that escapes after a double pass through the gain cell by energy conservation are related by

$$I_p = I_a + I_l \tag{38}$$

5.2 Small signal (no lasing) solutions

As an example of the numerical solution, we consider the baseline system of Table 1. These conditions approximate the quasi two-level limit for input pump intensities of less than 10 kW/cm². In some calculations we reduce the baseline number density of methane to show the effect on saturation behavior that results from the smaller upper level mixing rates. In these cases it is assumed that an appropriate amount of He is added to the mixture such that the pressure broadening and cross-sections are the same as the baseline. The broadband pump solutions are compared with the single-frequency pump solutions for the same cell conditions and for the same total power. By making the comparison in this way the effects that are directly related to the bandwidth of the pump can be compared. Parametric calculations with variations in the pump bandwidth are also made to show its effect on laser performance.

The small signal solutions for the negative gain (absorption) on the pump transition, $g^o31 = \sigma_{31}(n_3 - 2n_1)$, and the laser gain, $g^o21 = \sigma_{21}(n_2 - n_1)$, as functions of I_p, are shown in Fig. 6 for pump band widths of 19.73, 50, and 100 GHz. The gain and absorption curves have the same shape. The threshold gain for the baseline conditions, ($r = 0.2$ and $t = 0.975$), is 0.214 cm⁻¹. All of the curves reach threshold for input pump power exceeding ~ 0.5 kW/cm², significantly greater than the saturation intensity, $I_s = 32.7$/cm². As the pump bandwidth increases

the required total power to achieve the same degree of saturation increases. All of the gain curves approach the asymptotic limit for the small signal gain of ~ 1.42 cm^{-1} at an input pump power of ~ 1 kW/cm^2. The small signal gain is very large and the system is pumped to $g^{o}21/\alpha = 6.6$ times threshold, even for this high output coupling case.

The corresponding spectral distributions of the two-pass transmitted pump intensity, I_t, predicted by Eq. (36) for band widths of 19.73, 50, and 100 GHz for an input pump power of 1 kW/cm^2 are provided in Fig. 7. The power that is most effective in pumping the absorption transition is from the center of pump spectral distribution. As the bandwidth increases a larger fraction of the transmitted pump power occurs in the wings.

5.3 Lasing solutions

Shown in Fig. 8 is a set of parametric plots showing the useful output laser intensity as functions of input intensity for different pump bandwidths. The solutions converge to the single-frequency solution, as the pump bandwidth is significantly less than the absorption profile width. If the

pump band width is less than or equal to the D$_2$ absorption band width for these cell conditions, the broadband solutions are to within better than 97 % of the analytic single frequency result. The apparent slope efficiency definitely decreases as the pump bandwidth increases. Note that the slope for the single-frequency case is constant, whereas the slope for the 100 GHz case decreases monotonically with increasing pump power. The apparent decrease in slope efficiency is also reflected in the increase in threshold pump power. As the pump bandwidth increases, more intensity in the wings of the pump is transmitted through the cell without being absorbed. The curves with bandwidths greater than the absorption lineshape also exhibit minor curvature.

If the laser output intensity is measured or plotted as a function of the absorbed pump intensity, the results lay on a single curve, as predicted by Eq. (15). This single curve is represented by the quasi two-level analytic equations using quasi two-level limit number densities and the quasi two-level limit results of Eq. (34), and the results reported in Part I. [17]

Recent Rb laser experiments have characterized the output power as a function of cell temperature (alkali concentration, n) [11]. Experimental slope efficiencies of up to 76 % were achieved for a pulsed Rb-methane DPAL with pump intensities exceeding 120 kW/cm^2. For $T \leq 65$ °C, the gain is below threshold. The peak output is achieved at $T = 110$–140 °C, depending on pump rate. Further increases in cell temperature increase bleaching of the sample and become more demanding. At $T = 160$–200 °C the laser output goes to zero and all of the pump energy is expended without reaching the threshold condition. The present model adequately represents these important observations.
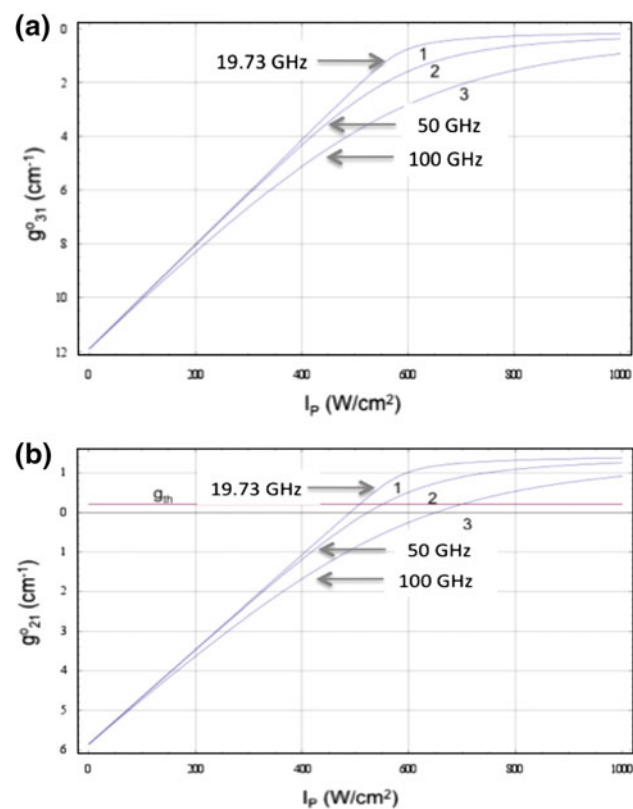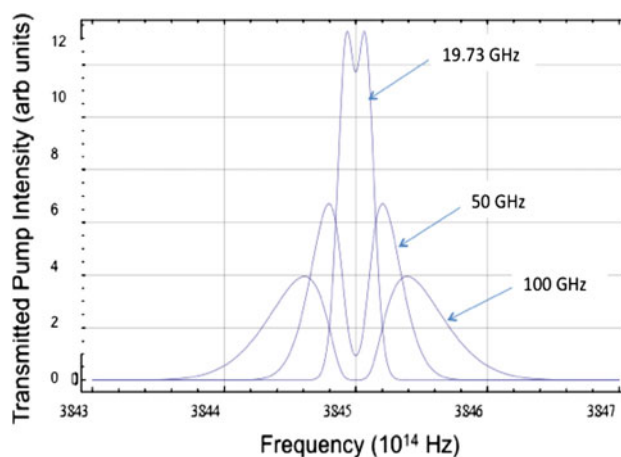

Fig. 6 Small signal gain on the **a** pump transition and **b** lasing transitions as a function of input pump intensity for three pump bandwidths of: 19.73, 50, and 100 GHz. Cell conditions are specified in Table 1

Fig. 7 Spectral distributions of the transmitted pump intensity, I_t, for small signal gain (no lasing) conditions, with bandwidths of: 19.73, 50, and 100 GHz. Cell conditions specified in Table 1, pump intensity of 1 kW/cm^2, double pass
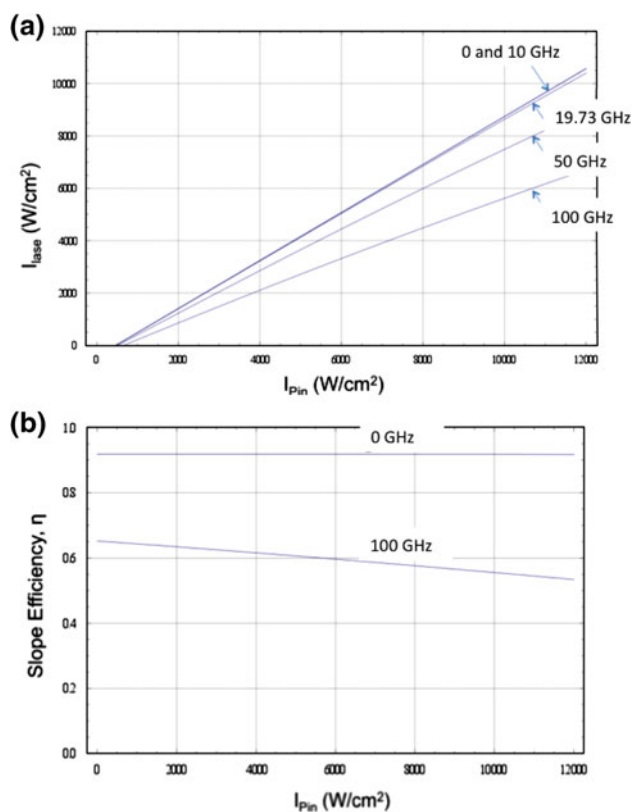
Fig. 8 **a** Output DPAL intensity as a function of incident intensity for (1) narrow-band pumping (0 GHz), 10, 19.73, 50 and 100 GHz. **b** Slope efficiency for narrow-band pumping (0 GHz) and $\Delta v_p = 100$ GHz. Cell conditions are specified in Table 1

The predicted optical-to-optical efficiency, I_L/I_p, as a function of cell temperature is shown in Fig. 9. The reduced absorption imposed by poorer matching of pump and absorption lineshapes can be accommodated by increased alkali vapor pressure. A modest decrease in device performance associated with increased threshold is minimized when the system is pumped at high intensity.

5.4 Comparison of numerical solutions with limiting cases

The predicted laser intensities for three fine-structure mixing rates (methane concentrations) are shown in Fig. 10 for the narrow-band pumping case. The slope and threshold for the baseline cell conditions take on their maximum and minimum values of 0.92 and 506.7 W/cm^2, respectively. For pump intensities of up to 60–70 % of the bleached limit, all three curves are well described by the linear quasi two-level prediction, Eq. (16). The slope decreases and approaches zero as the laser intensity converges to the maximum laser intensity in the bleached limit, Eq. (31).
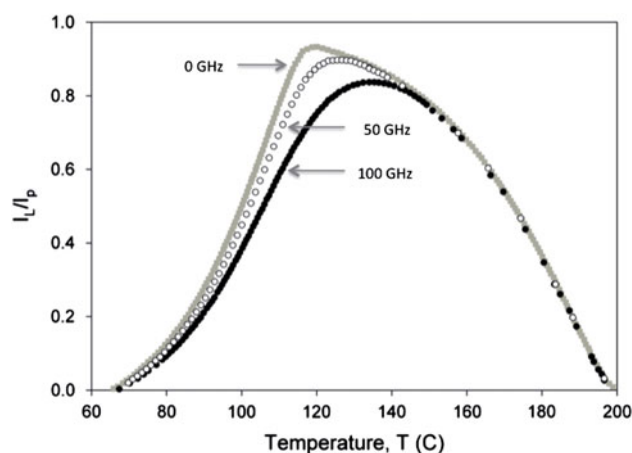

Fig. 9 Optical-to-optical efficiency, I_L/I_p, as a function of cell temperature (Rb vapor pressure) for pump linewidth, Δv_p, of: (*open squares*) 0, (*open circles*) 50 and (*filled circles*) 100 GHz

The maximum laser intensity lines increase with methane pressure because the maximum mixing rate is increasing.

5.5 Generalized absorption

The numerical solutions for broadband pumping can be organized by the absorption term, β, of Eq. (16). If this factor is established, then the general result can be derived from the Q2L limit. Indeed, the general numerical solution yields the product of the output intensity in the Q2L, and the absorption factor, β. This absorption is a complicated function of pump bandwidth, Δv_p, relative to the atomic absorption profile and the total alkali density, n.

Shown in Fig. 11 are plots of $\beta(\Delta v_p, n)$ verses Δv_p for several values of n, using the baseline parameters of Table I. We observe that the function $\beta(\Delta v_p, n)$ is approximately 1 for the baseline number density until the pump bandwidth exceeds the D$_2$ absorption line width. Beyond this point the absorption parameter decreases to a value of 0.73 for a pump bandwidth of 100 GHz. The maximum value region of $\beta(\Delta v_p, n)$, and hence the slope efficiency, can be extended by increasing the Rb number density as seen in curves (2), and (3) of Fig. 11. This is accomplished at the expense of increasing the threshold pump intensity, as discussed in Fig. 9.

A summary of the Rb DPAL performance for two bandwidths and two alkali concentrations is provided in Fig. 12. The numerical solutions are placed in context of the Q2L and bleached limits for each case. The results for the 20-GHz pump line width are nearly identical to the single-frequency results of Fig. 8, the deviation being due to the slight difference in slopes. The results for the 100-GHz pump are substantially different. The laser slope as predicted from the exact numerical solution begins to

Fig. 10 Comparison of numerical solutions for the conditions of Table 1 at three methane pressures with the quasi two-level and bleached limits
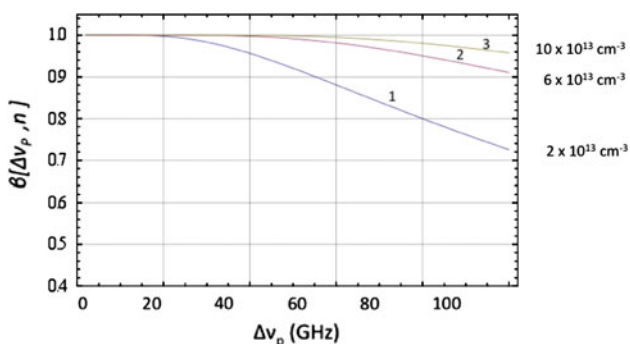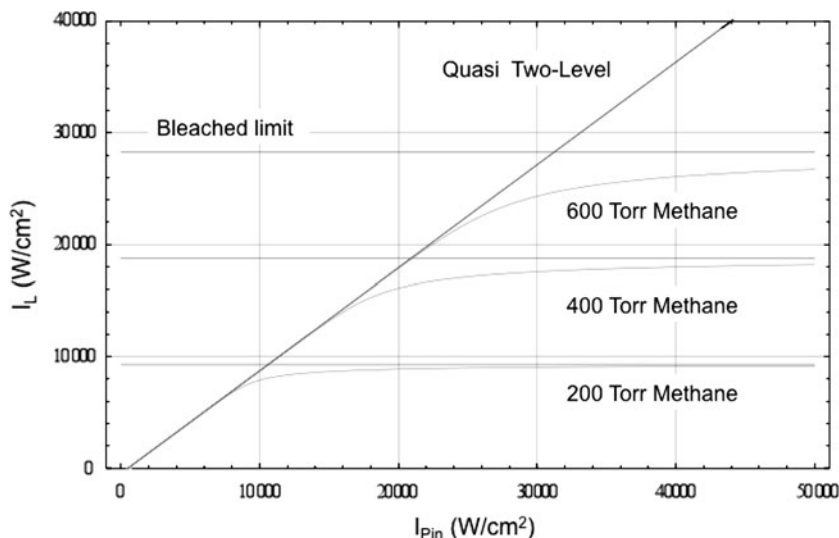

Fig. 11 Absorption factor, β, for rubidium concentrations of: 1 2.0×10^{13} cm^{-3}, 2 6.0×10^{13} cm^{-3}, and 3 1.0×10^{14} cm^{-3}

deviate from the linear quasi two-level approximation for input pump intensities well below 10 kW/cm^2. We also note that for this broadband case the rate of convergence of the laser power to the maximum laser power is very slow. As a final example, we show how linear behavior for input pump intensities in the range of 10–20 kW/cm^2 can be recovered by increasing the Rb number density. For a Rb number density of 6.0×10^{13} cm^{-3}, the maximum laser power has increased by over a factor of three due to the increased mixing rate. A similar result could be achieved by increasing the methane number density by a factor of three. The latter approach, however, would result in greatly reduced pressure broadened D_1 and D_2 cross-sections and a cell pressure of over 2 atm, whereas the former approach requires only a modest increase in cell temperature.

6 Conclusions

The diode-pumped alkali laser development path includes two strategies: (1) high-pressure gain cells (>10 atm) and
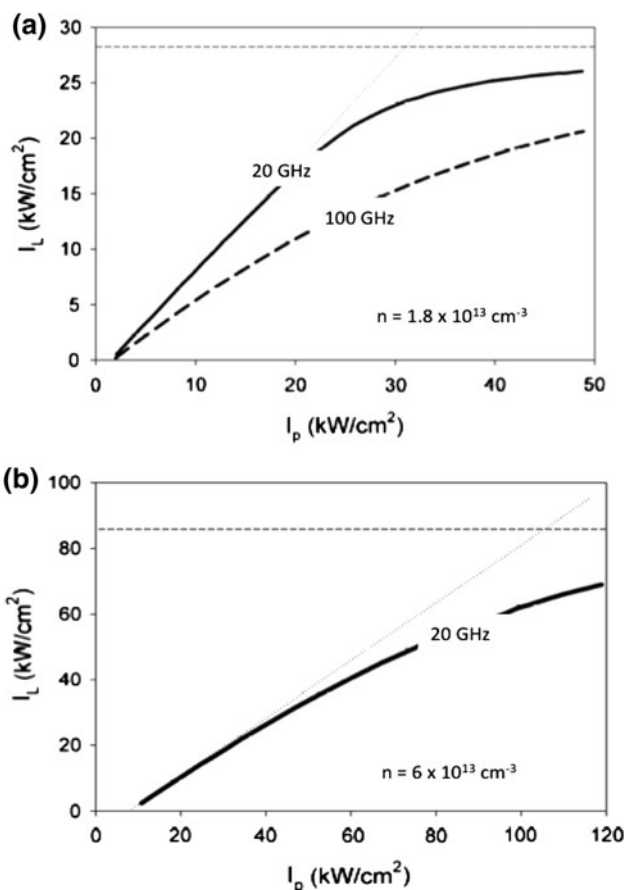

Fig. 12 Rb DPAL performance for: **a** rubidium concentration of 1.8×10^{13} cm^{-3} and two pump bandwidths: (*solid lines*) 20 GHz and (*dashed lines*) 100 GHz, and **b** rubidium concentration of 6.0×10^{13} cm^{-3} and 20 GHz bandwidth

diode bars with modest spectral narrowing (>100 GHz) or (2) low-pressure gain cells (~ 1 atm) and diodes with dramatic spectral narrowing (~ 10 GHz). In both cases, the

pump spectral width can be larger than the atomic absorption profile and still yield efficient operation. The DPAL slope efficiency decreases with increasing pump bandwidth for a given alkali concentration. However,

$$n_1^0(\Omega_f) \frac{2\gamma(hn\Gamma_{31}v_p - \Omega_f) + e^\theta(hn\Gamma_{21}(\gamma + \Gamma_{31})v_p - (\gamma + \Gamma_{21})\Omega_f)}{h(2\gamma\Gamma_{31} + e^\theta\Gamma_{21}(\gamma + \Gamma_{31}))v_p} \tag{39}$$

increasing the alkali concentration to obtain similar absorption can restore much of the performance. The threshold pump intensity does increase for higher alkali concentrations. All absorbed photons above threshold can be converted to output photons in the quasi two-level limit if the cavity is lossless, $T_c = 1$, and the resonator extraction is ideal. When the DPAL output intensity is measured against absorbed pump photons, rather than incident pump intensity, a single performance curve is observed.

The transition from the ideal quasi-two level performance at lower pump intensity to the fully bleached limit is sharp for narrow-band pumping. For pump widths of several times the pressure broadened atomic lineshape, the transition to full bleaching is more gradual. When the spin–orbit relaxation is rate limiting, the pump transition becomes fully bleached, excess pump intensity is transmitted, and output power is limited by the spin–orbit relaxation rate.

Appendix A: small signal and laser gain solutions

The solutions to the rate equations (2–5) in the absence of lasing provides the following small signal populations:

$$n_2^0(\Omega_f) = \frac{e^\theta \gamma \Omega_f}{h(2\gamma\Gamma_{31} + e^\theta\Gamma_{21}(\gamma + \Gamma_{31}))v_p} \tag{40}$$

$$n_3^0(\Omega_f) = \frac{(2\gamma + e^\theta\Gamma_{21})\Omega_f}{h(2\gamma\Gamma_{31} + e^\theta\Gamma_{21}(\gamma + \Gamma_{31}))v_p} \tag{41}$$

Combining Eqs. (39–41) we obtain expressions for the small signal gain/absorption on the pump and lasing transitions:

$$g_{31}^0(\Omega_f) = \frac{\sigma_{31}(v)(2\gamma(-2hn\Gamma_{31}v_p + 3\Omega_f) + e^\theta(-2hn\Gamma_{21}(\gamma + \Gamma_{31})v_p + (2\gamma + 3\Gamma_{21})\Omega_f))}{h(2\gamma\Gamma_{31} + e^\theta\Gamma_{21}(\gamma + \Gamma_{31}))v_p} \tag{42}$$

$$g_{21}^0(\Omega_f) = \frac{\sigma_{21}(v)(2\gamma(-hn\Gamma_{31}v_p + \Omega_f) + e^\theta(-2hn\Gamma_{21}(\gamma + \Gamma_{31})v_p + (2\gamma + \Gamma_{21})\Omega_f))}{h(2\gamma\Gamma_{31} + e^\theta\Gamma_{21}(\gamma + \Gamma_{31}))v_p} \tag{43}$$

The solutions to the rate equations (2–5) in the presence of lasing yields

$$n_1(\Omega_f)$$

$$= -\frac{2hg_{th}\gamma v_{31} + e^\theta(h(\gamma + \Gamma_{31})v_p(g_{th} - n\sigma_{21}) + \sigma_{21}\Omega_f)}{2h(\gamma + e^\theta(\gamma + \Gamma_{31}))v_p\sigma_{21}} \tag{44}$$

$$n_2(\Omega_f) = \frac{e^\theta(h(\gamma + \Gamma_{31})v_p(g_{th} + n\sigma_{21}) - \sigma_{21}\Omega_f)}{2h(\gamma + e^\theta(\gamma + \Gamma_{31}))v_p\sigma_{21}} \tag{45}$$

$$n_3(\Omega_f) = \frac{h\gamma v_p(g_{th} + n\sigma_{21}) + e^\theta\sigma_{21}\Omega_f}{h(\gamma + e^\theta(\gamma + \Gamma_{31}))v_p\sigma_{21}} \tag{46}$$

$$\Psi(\Omega_f) = \frac{v_{21}(2\gamma(-h\Gamma_{31}v_p(g_{th} + n\sigma_{21}) + \sigma_{21}\Omega_f) + e^\theta(-h\Gamma_{21}(\gamma + \Gamma_{31})v_p(g_{th} + n\sigma_{21}) + (2\gamma + \Gamma_{21})\sigma_{21}\Omega_f))}{2g_{th}(\gamma + e^\theta(\gamma + \Gamma_{31}))v_p\sigma_{21}} \tag{47}$$

Combining Eqs. (45) and (47) we obtain an expression for the gain/absorption on the pump transition under lasing conditions:

$$g_{31}(\Omega_f) = \frac{\sigma_{31}(v)(h\gamma v_p(3g_{th} + n\sigma_{21}) + e^\theta(h(\gamma + \Gamma_{31})v_p(g_{th} - n\sigma_{21}) + 2\sigma_{21}\Omega_f))}{h(\gamma + e^\theta(\gamma + \Gamma_{31}))v_p\sigma_{21}} \tag{48}$$

The gain on the lasing transition is clamped at its threshold value, g_{th}:

$$g_{21}(\Omega_f) = g_{th} = \frac{-\mathrm{Ln}[t^4 r]}{2l_g} \tag{49}$$

Appendix B: longitudinally averaged pump term, Ω_f

The first term on the right-hand side of Eq. (2) for the general broadband pumping case is given by the product of the absorption coefficient of the pump transition times the longitudinal two- way average $I_{Pavg}(v)$ of the pump intensity integrated over frequency.

$$\Omega_f = -\int_{-\infty}^{\infty} \sigma_{31}(v)(n_3 - 2n_1)I_{Pavg}(v)dv \tag{50}$$

Note that the following partial differential equation is satisfied whether the number densities depend on z or not:

$$\frac{\partial I(v,z)}{\partial z} = \sigma_{31}(v)(n_3 - 2n_1)I(v,z) \tag{51}$$

Assuming longitudinal averaged number densities that are independent of z, a particular solution to Eq. (51) satisfying a specified initial condition at $z = 0$ is given by

$$I(v,z) = I_{Pin}f_p(v)e^{\sigma_{31}(v)(n_3 - 2n_1)z} \tag{52}$$

In Eq. (52), we have assumed a flat top intensity profile, I_{Pin}, for the total input pump intensity and that $f_p(v)$ is the normalized spectral distribution of the pump. The term $I_{Pavg}(v)$ in Eq. (50) is evaluated using the same procedure as in Part I, [17]. Assuming the window transmission coefficient and reflectance of the right folding mirror, (Fig. 1) are both one at the D_2 wavelength, I_{Pavg} is given by:

$$I_{Pavg}(v) = \frac{1}{l_g}\left(\int_0^{l_g}(I^+(v,z) + I^-(v,z))dz\right) \tag{53}$$

$$= \frac{1}{l_g}\left(I_{P0}^+\int_0^{l_g}e^{\sigma_{31}(v)(n_3 - 2n_1)z}dz + I_{P0}^-\int_0^{l_g}e^{\sigma_{31}(v)(n_3 - 2n_1)(l_g - z)}dz\right)$$

where $I_{P0}^+ = I_{Pin}f_p(v)$ and $I_{p0}^- = I_{Pin}f_p(v)e^{\sigma_{31}(v)(n_3 - 2n_1)l_g}$ performing the indicated integration in Eq. (53) using the initial conditions for the right and left propagating pump waves we obtain

$$I_{Pavg}(v) = I_{Pin}f_p(v)\left[\frac{e^{\sigma_{31}(v)(n_3 - 2n_1)2l_g} - 1}{\sigma_{31}(v)(n_3 - 2n_1)l_g}\right] \tag{54}$$

Substituting Eq. (54) into Eq. (50), canceling common terms, and writing the number densities as explicit functions of Ω_f, we obtain

$$\Omega_f = \frac{I_p}{l_g}\left(\int_{-\infty}^{\infty} f_p(v)e^{\sigma_{31}(v)(n_3(\Omega_f) - 2n_1(\Omega_f))2l_g}dv - 1\right) \tag{55}$$

Equation (55) is Eq. (6) of the text.

References

1. W.F. Krupke, R.J. Beach, V.K. Kanz, S.A. Payne, Opt. Lett. **28**, 2336 (2003)
2. J. Zweiback, B. Krupke, Proc. SPIE **7581**, 75810G (2010)
3. A.V. Bogachev, S.G. Garanin, A.M. Dudov, V.A. Yeroshenko, S.M. Kulikov, G.T. Mikaelian, V.A. Panarin, V.O. Pautov, A.V. Rus, S.A. Sukharev, Quantum Electron. **42**, 95–98 (2012)
4. B.V. Zhdanov, T. Ehrenreich, R.J. Knize, Opt. Commun. **260**, 696 (2006)
5. T. Ehrenreich, B.V. Zhdanov, T. Takekoshi, S.P. Phipps, R.J. Knize, Electron. Lett. **41**, 415 (2005)
6. R.J. Beach, W.F. Krupke, V.K. Kanz, S.A. Payne, J. Opt. Soc. Am. B. **21**, 2151 (2004)
7. A. Gourevitch, G. Venus, V. Smirnov, D.A. Hostutler, L. Glebov, Opt. Lett. **33**, 702 (2008)
8. J.F. Sell, W. Miller, D. Wright, B.V. Zhdanov, R.J. Knize, Appl. Phys. Lett. **94**, 051115 (2009)
9. C.S. Sulham, G.P. Perram, M.P. Wilkinson, D.A. Hostutler, Opt. Commun. **283**, 4328 (2010)
10. W.S. Miller, C.V. Sulham, J.C. Holtgrave, G.P. Perram, Appl. Phys. B **103**, 819–824 (2011)
11. N.D. Zameroski, G.D. Hager, W. Rudolph, D.A. Hostutler, J. Opt. Soc. Am. B **28**, 1088 (2011)
12. J. Zweiback, G.D. Hager, W.F. Krupke, Opt. Commun. **282**, 1871 (2009)
13. W.F. Krupke, R.J. Beach, V. Keith Kanz, S.A. Payne, J.T. Early, Proc. SPIE **5448**, 7 (2004)
14. Zining Yang, Hongyan Wang, Lu Qisheng, Yuandong Li, Weihong Hua, Xu Xiaojun, Jinbao Chen, J. Opt. Soc. Am. B **28**, 1353 (2011)
15. Zining Yang, Hongyan Wang, Lu Qisheng, Liang Liu, Yuandong Li, Weihong Hua, Xu Xiaojun, Jinbao Chen, J. Phys. B: At. Mol. Opt. Phys. **44**, 085401 (2011)

16. Qi Zhu, Bailiang Pan, Li Chen, Yajuan Wang, Xunyi Zhang, Opt. Commun. **283**, 2406 (2010)
17. G.D. Hager, G.P. Perram, Appl. Phys. B **101**, 45 (2010)
18. P. Peterson, A. Gavrielides, P.M. Sharma, Opt. Commun. **109**, 282 (1994)
19. R.J. Beach, Opt. Commun. **123**, 385 (1995)
20. N.D. Zameroski, W. Rudolph, G.D. Hager, D.A. Hostutler, J. Phys. B: At. Mol. Opt. Phys. **42**, 245401 (2009)
21. D.A. Steck, 2008 Rubidium 87 D line data. http://steck.us/alkalidata
22. M.D. Rotondaro, G.P. Perram, Phys. Rev. A **57**, 4045 (1998)
23. M.D. Rotondaro, G.P. Perram, J. Quant. Spectrosc. Radiat. Transf. **57**, 497 (1997)
24. G.A. Pitz, G.P. Perram, SPIE Proc. **7005**, 700526 (2008)